Perovskite-based Phase Transition Sorbents for Sorption Enhanced Oxidative Steam Reforming of Glycerol

Leo Brody[1,‡], Runxia Cai[1,‡], Alajia Thornton[1], Junchen Liu[1], Hao Yu[2], and Fanxing Li[1,*]

[1.] Department of Chemical and Biomolecular Engineering, North Carolina State University, Raleigh, NC 27695-7905

[2.] School of Chemistry and Chemical Engineering, South China University of Technology, Guang Zhou, China 510641

‡ Co-first authors

* *Correspondence author: fli5@ncsu.edu*

Abstract

Sorption enhanced steam reforming represents an efficient strategy to produce concentrated hydrogen from superfluous carbonaceous feedstocks. However, commonly used CaO-based sorbents are prone to sintering, leading to a rapid loss in CO_2 sorption capacity and activity under repeated reaction cycles. Herein, we report perovskite-based phase transition sorbents (PTSs) capable of avoiding sintering and retaining both catalytic activity and sorption capacity. Specifically, A- and B-site doped $SrFeO_{3-\delta}$, i.e., $Sr_{1-x}Ca_xFe_{1-y}Ni_yO_{3-\delta}$, were evaluated as PTSs for the sorption enhanced – steam reforming of glycerol (SESRG). Packed bed reactor experiments were performed in conjunction with redox, bulk, surface, and morphology characterizations to evaluate SCFNs' performance and the underlying phase transition scheme. These characterizations revealed that reduced oxides from the A-site of the PTS (SrO, CaO) are carbonated during the reforming step before reversibly undergoing decarbonation at a higher temperature under an oxidizing environment. This study demonstrates that SCFN is a tri-functional material capable of (i) catalyzing the reforming of glycerol; (ii) absorbing CO_2 *in-situ*; and (iii) reversibly releasing oxygen from lattice sites to enhance glycerol conversion. While all the screened compositions achieved >87 vol% pre-breakthrough H_2 purities, SCFN-4691($Sr_{0.4}Ca_{0.6}Fe_{0.9}Ni_{0.1}O_{3-\delta}$) and SCFN-5591 ($Sr_{0.5}Ca_{0.5}Fe_{0.9}Ni_{0.1}O_{3-\delta}$) showed particularly high (95.6-97.3%) H_2 purities with stable CO_2 sorption capacities.

Keywords: Syngas, Perovskite oxides, Sorption-enhanced steam reforming, Phase transition sorbents

Introduction

Hydrogen (H_2) is rapidly gaining attention as an eco-friendly energy carrier, especially when produced from sustainable feedstocks such as biomass [1]. Currently, hydrogen is primarily produced from methane reforming followed by water-gas shift (WGS), acid gas removal, and purification, which consume substantial amount of energy [2-5]. A green feedstock alternative may be found in crude glycerol – a low-value byproduct from biodiesel production [6]. Methods of producing hydrogen or syngas from glycerol include pyrolysis [7, 8], steam reforming [9, 10], aqueous-phase reforming [11], and autothermal reforming [12, 13]. Akin to the reforming of hydrocarbons,

glycerol reforming is an endothermic process that produces syngas at 650-800 ˚C (Equation 1) [14]. When steam is co-fed in excess, the co-occurring WGS reaction can further oxidize CO to CO_2 (Equation 2) resulting in a less endothermic overall reaction represented by Equation 3. At lower temperatures, methanation can also occur via Reaction 4. The reforming of glycerol, however, is challenged by low conversion, high endothermicity, poor H_2 selectivity, and an appreciable tendency for coke formation [15-17]. Oxidative steam reforming (Equation 5) can lower the energy requirement for reforming and inhibit some undesirable side reactions but does so at the expense of H_2 yield [18].

$$C_3H_8O_3 \leftrightarrow 3CO + 4H_2 \ \ (\Delta H_r^0 = +250\ \text{kJ} \cdot \text{mol}^{-1}) \tag{1}$$

$$CO + H_2O \leftrightarrow CO_2 + H_2 \ \ (\Delta H_r^0 = -41\ \text{kJ} \cdot \text{mol}^{-1}) \tag{2}$$

$$C_3H_8O_3 + 3H_2O \leftrightarrow 3CO_2 + 7H_2 \ \ (\Delta H_r^0 = +128\ \text{kJ} \cdot \text{mol}^{-1}) \tag{3}$$

$$CO + 3H_2 \leftrightarrow CH_4 + H_2O \ \ (\Delta H_r^0 = -206\ \text{kJ} \cdot \text{mol}^{-1}) \tag{4}$$

$$C_3H_8O_3 + (3-\delta)H_2O + \frac{\delta}{2}O_2 \leftrightarrow 3CO_2 + (7-\delta)H_2 \tag{5}$$

Carrying out both the reforming and WGS reaction simultaneously can improve conversion but lowers H_2 concentration due to the substantial amount of CO_2 produced. This steam reforming process can be intensified through a sorption enhancement effect whereby CO_2 produced from the WGS reaction is removed *in-situ* – shifting the WGS reaction equilibrium toward H_2 production [19-23]. This is achieved through the use of CO_2 sorbents (e.g., CaO), which fix the gaseous CO_2 produced from the WGS reaction into carbonates (Reaction 6). The carbonates formed are subsequently decarbonated at a higher temperature. The effect of introducing sorbents can significantly increase the H_2 concentration [24, 25] and suppress unwanted side-reactions such as methanation and coke formation [26]. Summing the pyrolysis, WGS, and carbonation reactions yields the overall sorption enhanced steam reforming of glycerol (SESRG) scheme (Reaction 7).

$$CaO + CO_2 \leftrightarrow CaCO_3 \ \ (\Delta H_r^0 = -178.3\ \text{kJ} \cdot \text{mol}^{-1}) \tag{6}$$

$$C_3H_8O_3 + 3H_2O + 3CaO \leftrightarrow 3CaCO_3 + 7H_2 \ \ (\Delta H_r^0 = -407\ \text{kJ} \cdot \text{mol}^{-1}) \tag{7}$$

A persistent obstacle in the area of sorption-enhanced steam reforming is the observed loss of sorption capacity caused by the structural degradation, or sintering, of sorbents during the high temperature decarbonation step. Commonly used CaO-based sorbents suffer a 40-60% decrease in CO_2 absorption capacity within the first 10 reaction cycles [27-29]. With a Tammann temperature of only ~533 ˚C [28], $CaCO_3$ particles sinter even during the lower temperature reforming step (550-600 ˚C), resulting in the formation of a $CaCO_3$ shell around the CaO core – preventing diffusion of CO_2 to the sorbent [30]. Previous attempts to resolve this problem have included decreasing sorbent particle size [31, 32], introducing inert refractory materials (e.g., calcium aluminates) as physical spacers [33-36], and the designing of "smart" catalysts capable of undergoing reversible phase changes at high temperatures to avert sintering [37]. While the first two strategies yielded some marginal improvement in prolonging CO_2 sorption, the overall effectiveness of the processes was reduced due to the inert spacers and supports. The third approach to inhibit sorbent deactivation encompasses the design of phase reversible, multi-functional materials. This is

particularly promising given the materials' ability to avoid sintering without compromising sorption capacity or catalytic activity. The first demonstration of a temperature-induced phase transition sorbent (PTS) came from a study by Zhao et al. investigating polymorphic Ca_2SiO_4 – a material capable of changing its volume during temperature swings and maintaining stable CO_2 sorption capacities for >15 Ca-looping cycles [38]. More recent are the results of Dang et al. whose support-free, calcium cobaltate ($Ca_xCo_{1-x}O$) material displayed excellent stability over 120 reaction-decarbonation cycles and achieved ~95% H_2 purity via SESRG [25]. By introducing air in their decarbonation step, Dang and his co-workers rendered this reaction highly exothermic. This is in stark contrast with the previously observed endothermic regenerations. Other bifunctional PTS systems have been proposed without Ca, such as the Ce stabilized Ni-SrO catalytic PTS published by Gu et al. for sorption enhanced methane reforming [39]. While the results from these studies are promising, systematic investigations of the PTS materials, their multifunctional characteristics, and design strategy have not been performed.

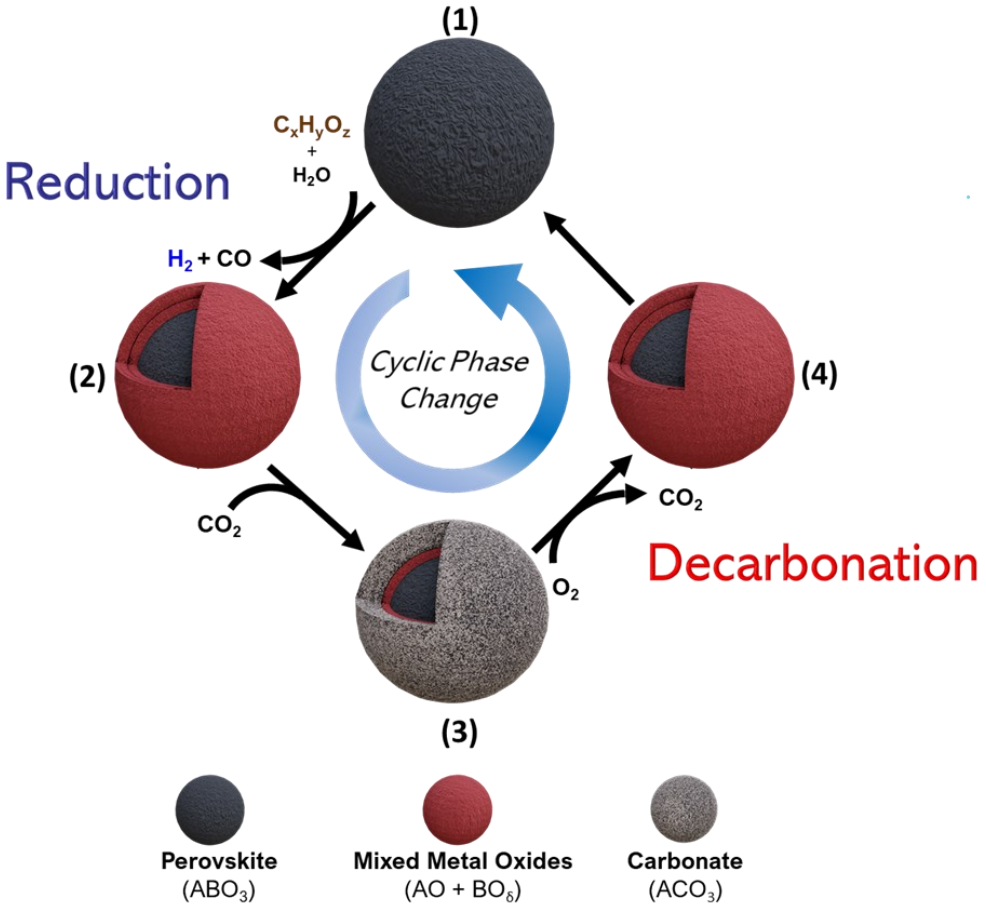

Figure 1. A simplified schematic of the perovskite-based phase transition cycle. In Step 1 to 2, perovskite is reduced in the presence of an oxygenated hydrocarbon (e.g., glycerol) to mixed A-and B-site oxides of varying reduction extent signified by δ. In Step 2 to 3, the A-site oxides are subsequently carbonated from CO_2 produced by the WGS reaction (not shown). Introducing oxygen and a temperature swing decarbonates the PTS (Steps 3 to 4) before finally regenerating the depleted oxygen lattice and returning to the perovskite phase.

What is clear is that an ideal PTS for SESRG should (i) be catalytically active for C-C cleavage and the WGS reaction; (ii) have a high CO_2 sorption capacity; (iii) maintain activity and sorption

capacity over repeated reaction cycles (i.e., good longevity); and (iv) undergo recyclable phase changes within each reaction cycle to avoid sintering, or a permanent transition to a less than ideal structure. This motivates the use of perovskite oxides, with the general formula $ABO_{3-\delta}$ (where the A cation is typically an alkali or alkaline earth metal, the B cation is a transition metal, and the delta is the oxygen non-stoichiometry), represent a durable, redox active, and highly tunable class of materials due to the ease at which their A-and B-sites can be doped with foreign cations for fine-tuning of redox kinetic and thermodynamic behavior [40-42]. The value of the non-stoichiometry term δ is a function of temperature and partial pressure of oxygen (p_{o2}), and its change ($\Delta\delta$) dictates how much oxygen is donated from the lattice sites as well as the B-site cation's extent of reduction [40-43]. Doping the B-site with foreign cations of differing oxidation states or ionic radii can induce oxygen vacancies in the lattice sites and thus impact redox performance [40]. The A-site can be populated with different sized cations to vary structural quality, as has been shown in previous studies investigating doped strontium ferrite ($SrFeO_{3-\delta}$) for chemical looping air separation and oxidative uncoupling [40, 44-46]. The proven recyclability of perovskite oxides in previous chemical looping schemes suggests that these materials may serve as suitable PTSs for a wide range of applications including SESRG [47].

We hypothesize that doped perovskite oxides can behave as PTSs as shown schematically in Figure 1. To test this, we have subjected various compositions of $Sr_{1-x}Ca_xFe_{1-y}Ni_yO_{3-\delta}$ (SCFN) to cyclic SESRG reactions to assess its performance as a PTS. Relevant performance metrics include glycerol conversion, pre-breakthrough time (t_{pb}), CO_2 storage capacity, oxygen donation ($\Delta\delta$), stability over repeated cycles, and H_2 purity witnessed during the pre-breakthrough and post-breakthrough stages of the reduction step. Various characterization methods were employed to obtain morphological, redox, bulk, and surface chemical properties to elucidate the dynamic phase changes throughout the process.

Experimental Section

Synthesis of SCFN materials

The perovskite-based PTS particles were synthesized via the modified Pechini method whereby the perovskite phase was formed after calcination of a polymeric resin containing the A-and-B-site metal cations. Summarily, an aqueous solution containing stoichiometric ratios of the desired metal cations (Sr^{2+}, Ca^{2+}, Fe^{3+}, Ni^{2+}) was prepared by dissolving their corresponding nitrates at room temperature. The solution was heated to 40˚C and citric acid was then added to form a metallic citrate before undergoing further heating to 80 ˚C, where ethylene glycol was introduced (at a 3:2 molar ratio of ethylene glycol to citric acid) to esterify the metallic citrate into a polymeric resign (i.e., polyester). After ~3 hours of isothermal mixing, the newly formed gel was then placed in an oven at 120 ˚C for 16 hours before subsequent calcination in air for 10 hours at 1000 ˚C in a muffle furnace. The resulting solids were then ground with a mortar and pestle and sieved to particle diameters within the range of 180-250 μm. Herein, $Sr_{1-x}Ca_xFe_{1-y}Ni_yO_{3-\delta}$ represents the Sr molar fraction of x in the A-site and Fe molar fraction of y in the B-site.

SESRG experiments

The SESRG experiments were performed in a quartz U-tube fixed bed reactor with an 8 mm I.D. and length of 280 mm (Figure 2). The quartz U-tube was housed in a Carbolite tube furnace for temperature control with looped temperature cycling controlled and automated via PLATINUM^{TM} Configurator software (Omega Engineering). A 50 mL stainless steel syringe filled with 30 wt.% glycerol in water was propped on a programmable injection platform automated via FlowControl^{TM} software (Harvard Apparatus) to cyclically inject the feedstock at 0.02 mL·min^{-1}. A PTFE line with a 1/16'' O.D. connected the terminal of the syringe to a two-way liquid injector valve automated with an electronic actuator (VICI Valco Instruments) and programmed with LABVIEW. A 1/16'' O.D. PTFE line connected the outlet of the valve to a stainless-steel capillary tube which fed into the U-tube reactor. The reactor was packed with 1.0 g of PTS material, and with quartz wool and silicon carbide used as inert packing material to prevent blowout as well as preheat the inlet gas. A 1/8'' O.D. stainless steel line connected the outlet of the reactor to a condenser U-tube submerged in a beaker of chilled water to separate any unreacted glycerol and water. The gaseous stream exiting the condenser was then fed to a MKS Cirrus II quadrupole mass spectrometer (QMS) for real-time stream composition analysis. The flowrates of purge and oxidizing gasses were regulated via Alicat MFCs, with valve-switching controlled by NI MAX (National Instruments^{TM}). Throughout the reaction cycles, a constant stream of 30 SCCM Ar (Airgas UHP 5.0 grade) was flowed to facilitate the movement of gaseous products through the system as well as to act as a purge gas between the reforming and decarbonation steps. During the decarbonation step, 3.30 SCCM of O_2 (Airgas extra dry grade) was injected to maintain a 10% O_2 atmosphere. The 65-minute reaction cycle comprised a 20-minute reforming step and a 20-minute decarbonation step and proceeds as follows: (1) 20-minute injection of glycerol/water mixture at 570 ˚C; (2) 10-minute isothermal purge with Ar; (3) 10-minute ramp with O_2/Ar from 570 to 850 ˚C; (3) 10-minute isothermal oxidation; (4) 15-minute ramp back down to 570 ˚C under Ar.

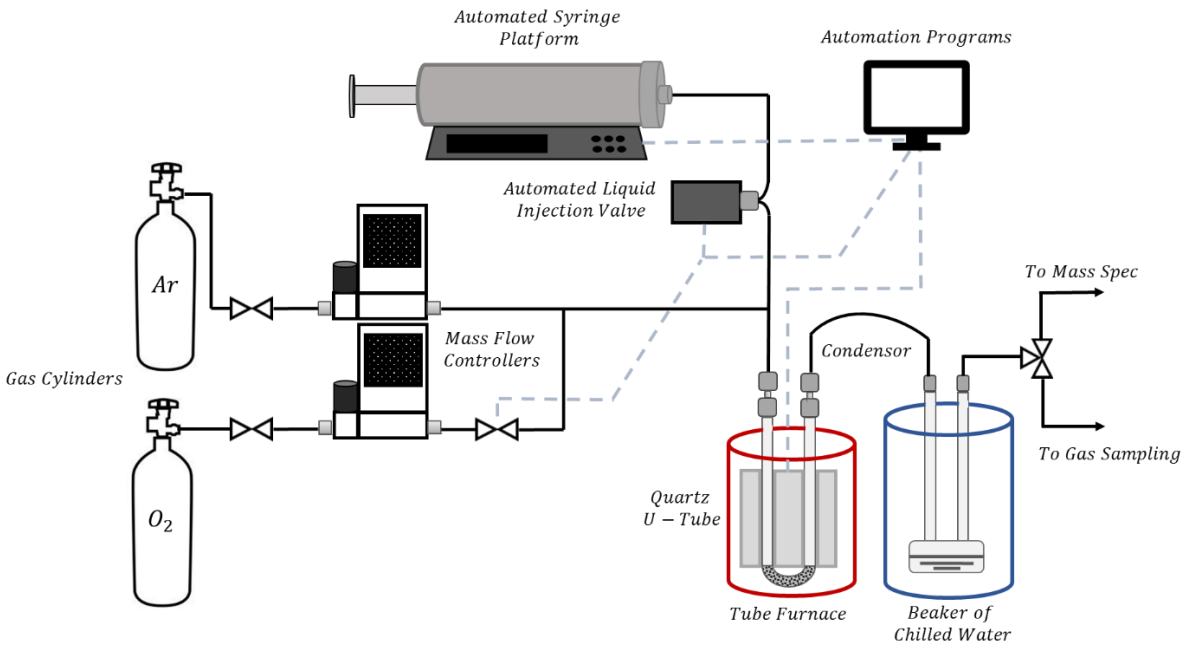

Figure 2. The SESRG experimental setup.

SESRG gaseous products were sampled within the first minute of the pre-breakthrough period as well as the last two minutes of the post-breakthrough period. The gas samples were analyzed using an Agilent 7890 Series Fast RGA gas chromatograph (GC) with two thermal conductivity detector (TCD) channels (He/TCD channel for CO/CO_2 analysis, Ar/TCD channel for H_2 analysis), and a flame ionization detector (FID) channel for hydrocarbon analysis.

Values of t_{pb}, CO_2 sorption capacities (Equation 8), and time averages of H_2 vol% over the reduction steps were obtained from MS data, while the pre-and post-breakthrough H_2 concentrations (Equation 9) were measured via GC. The CO_2 sorption capacity was determined by dividing the measured moles of CO_2 released in the decarbonation step by the known moles of SCFN (Equation 8). To put it in perspective, a 30% CO_2 sorption capacity in SCFN 5591 corresponds to 8.2 wt.% weight based sorption capacity when normalized with the initial weight of the sorbent. Since the volume of injected glycerol was carefully controlled (0.4 mL), glycerol conversion X_G (Equation ES1) could be calculated via a carbon balance using the MS signals of CO_x and CH_4 species.

$$CO_2\ Sorption\ Capacity = \left(\frac{n_{CO_2 released}}{n_{SCFN}}\right) \times 100 \quad (8)$$

$$H_2\ Purity = \left(\frac{[H_2]}{[H_2]+[CO_2]+[CH_4]+[CO]}\right) \times 100 \quad (9)$$

Determination of sorption capacity and oxygen non-stoichiometry

Two sets of experiments were carried out using thermogravimetric analyzers equipped with differential scanning calorimeters (TGA, TA Instruments SDT Q600): (1) cyclic reactions using CO_2 and H_2 as the feeds for the reduction step with concentrations approximating SESRG reactor conditions; and (2) stepwise temperature changes from 500-900 ˚C under varying concentrations of oxygen. For the first experiment, ~50 mg of SCFN particles (180-250 μm) were loaded into an alumina crucible cell within the TA instrument and then heated to 570 ˚C with a ramping rate of 20 ˚C/min under Ar. The flowrates of gasses fed to the TA instrument were controlled using Alicat MFCs, akin to our reactor setup. To simulate the simultaneous reducing and carbonating environment of the reduction step in the packed bed experiments, the inlet volumetric concentrations of H_2 and CO_2 and the balance Ar for the TGA reduction steps were obtained from MS data with the same SCFN composition (Table S1). The reduction/carbonation step was performed at 570 ˚C for 20 min, with a 11min Ar purge following. The temperature of the cell was maintained for another 3 min with the gas switching from pure Ar to 40% O_2 flow. The system was then heated to 850 ˚C for the decarbonation/regeneration step with continual, O_2/Ar flow for 25 min. After a final 16 min Ar purge, the redox cycle was repeated. Figure S1 in the SI file illustrates a typical TA profile of a reduction/decarbonation reaction cycle.

In the second TGA experiment, ~50 mg of SCFN was heated to 700 ˚C under 50% O_2/Ar and held isothermal for 20 min before being cooled down to 500 ˚C. The sample was then heated stepwise at 20 ˚C/min from 500-900 ˚C with 10 min isotherms every 50 ˚C. These temperature steps were repeated for 20%, 10%, 5%, 3%, 1% O_2/Ar concentrations and pure Ar. Upon completion of the last temperature cycle under Ar, the sample was ramped to 1100 ˚C under 20% H_2/Ar to fully

reduce the sample in order to establish a baseline. The combined results of both experiments were used to determine the non-stoichiometry (δ) and the CO_2 sorption capacity of various SCFN compositions under cyclic redox cycles. The TGA reaction cycle profiles (Figure S1) reveal a clear mass gain due to carbonation during the reduction step, with a second distinct mass increase after the purge due to oxygen replenishing the depleted lattice sites. Therefore, $\Delta\delta$ was obtained directly from TGA data by taking the mass difference (Δm_s) of the pre-and post-oxygen regenerated samples after the purge step (Equation 10).

$$\Delta\delta = \frac{\Delta m_s \cdot M_{SCFN}}{M_{O_2} \cdot m_{SCFN}} \tag{10}$$

SCFN phase, morphology, and surface characterization

Bulk phase identification was conducted using both *ex-situ* and *in-situ* X-ray diffraction characterization. Fresh, reduced, and regenerated SCFN samples taken from both TGA and SESRG reactor experiments were analyzed with *ex-situ* XRD. A Rigaku SmartLab X-ray diffractometer with Cu Kα (λ = 0.1542 nm) radiation operating at 40 kV and 44 mA was used. A scanning range of 10-60˚ (2θ) with a step size of 0.1˚ holding for 3.5 s at each step was used to generate XRD patterns. In order to assess dynamic phase change of the SCFN material under a regenerating/decarbonating gas atmosphere, *in-situ* XRD was carried out using an Empyrean PANalytical XRD using Cu Kα radiation operating at 45 kW and 40 mA. A scanning range of 10-60˚ (2θ) was at a ramp rate of 0.1˚ holding for 0.1 s at each step. Temperature-programmed experiments were conducted on two samples of SCFN-5591 pre-treated either with only 17.75% H_2 balance Ar or 17.75% H_2 and 4.75% CO_2 balance Ar. In both *in-situ* XRD experiments, the samples were heated in N_2 at 5 ˚C·min^{-1} to 570 ˚C, after which 10% O_2/N_2 was introduced while ramping the temperature up to 850 ˚C at the same rate. After holding isothermal at 850 ˚C for 30 min, the sample was then cooled down to ambient temperature under pure N_2.

XPS was used to analyze surface compositions and valence states of fresh and reduced SCFN-5591 samples. The sample powders were pressed onto carbon tape and outgassed at 10^{-5} Torr overnight before being introduced into the ultrahigh-vacuum chamber for scanning. The XPS patterns were collected on a PHOIBOS 150 hemispherical energy analyzer (SPECS GmbH) equipped with a non-monochromatic Mg Kα excitation source (1254 eV). The resulting data were analyzed in the CasaXPS program (Casa Software Ltd). The binding energy was calibrated to a C 1s line at 285 eV. The surface compositions of Sr, Ca, Fe, Ni, O, and C were calculated according to characteristic peak areas and their respective atomic sensitivity factors. After calibration, the background from each spectrum was subtracted using a Shirley-type background. XPS peak locations, FWHM values, and area percentages can be found in Table S3 in the SI file.

Surface morphology and elemental distribution were assessed via field emission scanning electron microscopy (FSEM) and energy-dispersive spectroscopy (EDS) using an Oxford X-Max system at an accelerating voltage of 15 kV and working distance of 8.5 mm. Additionally, the BET surface area and BJH pore volume distribution of both fresh and cycled SCFN-5591 samples were measured at 77 K with a physisorption apparatus (Micrometrics ASAP 2020) via a multipoint physical measurement.

Results and Discussion

SESRG performance of SCFN

Overall SESRG performance results for each SCFN composition are presented in Figure 3(b), with individual performances by cycle number displayed in Figure S2 and Table S2 in the supporting information (SI) file. For all the compositions screened, the pre-breakthrough H_2 purity, sorption capacity, and t_{pb} remain stable over 15 cycles, which is beyond the point where a significant decrease in sorption capacity occurs for CaO-based sorbents (~10 cycles). All the screened compounds also achieved an H_2 selectivity higher than equilibrium selectivity (Figure S3).

From the 15 cycle runs shown in Figure 3(b), it is apparent that, from a pure H_2 production standpoint, the best performing material was SCFN-5591 with an average pre-breakthrough H_2 purity of ~97% and an average t_{pb} of 2.50 min. However, SCFN-4691 outperformed SCFN-5591 in sorption capacity and H_2:CO ratio. This result implies a nonlinear relationship between t_{pb} and sorption capacity, and more rigorous mechanistic studies will be needed to uncover what transport and kinetic effects link these two quantities. Interestingly, doping the A-site with less than 50% Ca leads to a decrease in glycerol conversion, likely due to the relatively higher stability of $SrFeO_{3-\delta}$ in comparison to $CaFeO_{3-\delta}$. Such a trend can be understood by considering the Goldschmidt tolerance factor $\tau = r_{A-O}/\sqrt{2r_{B-O}}$ for the generic perovskite ABO_3, which predicts the stability of the perovskite species based on its proximity to an ideal cubic structure ($\tau = 1$) [48]. The smaller ionic radius of Ca^{2+} compared to Sr^{2+} distorts the BO_6 octahedra, resulting in a lower tolerance factor and hence diminished stability [49]. Considering its excellent performance, SCFN-5591 was subjected to twice as many reaction cycles. As can be seen in Figure 3(c), the sorption capacity plateaus at ~35% after the first 10 cycles and remains stable after 35 cycles. This initial increase and subsequent stabilization of sorption capacity could be linked to changes in pore size distribution.

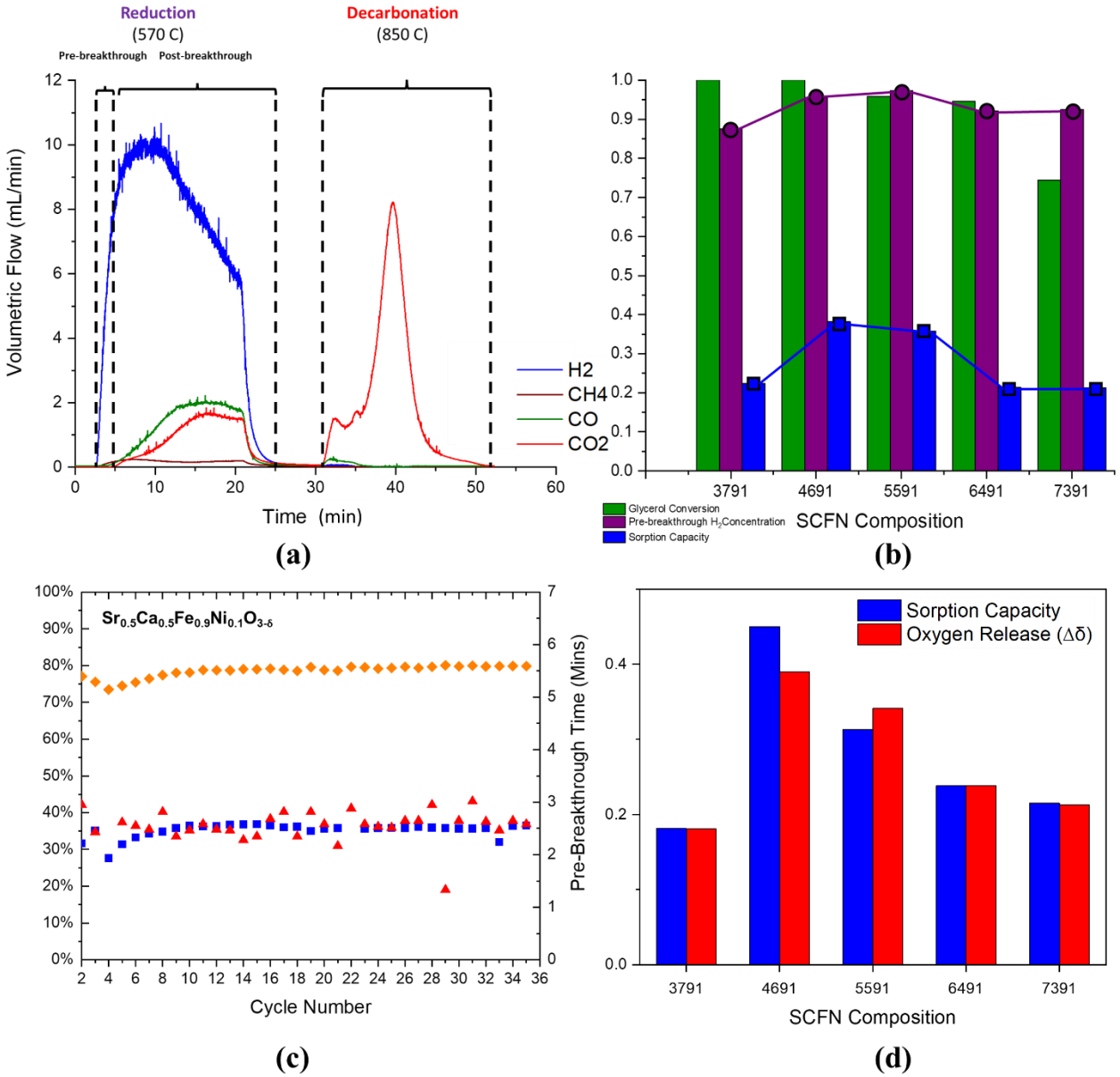

Figure 3. (a) A characteristic reaction cycle taken from SCFN-5591 MS data (H_2O and Ar not shown). The reduction step, which occurs at 570˚C, encompasses both the pre-and-post-breakthrough periods. The decarbonation/regeneration step releases nearly pure CO_2 when using O_2 as the oxidizing gas; (b) Summary of SESRG performance across SCFN composition with glycerol conversion (green), pre-break H_2 concentration (purple), and sorption capacity (blue); (c) Stable SESRG reactor performance of SCFN-5591 with reduction step H_2 volumetric concentrations (yellow diamonds), CO_2 sorption capacity (blue squares), and pre-breakthrough times (red triangles); (d) Average CO_2 sorption capacity and oxygen release ($\Delta\delta$) comparisons samples for all five SCFN compositions subjected to 15 TGA reaction cycles.

Lattice oxygen release and CO_2 uptake are both a function of B-site reduction, thus the measured oxygen release values ($\Delta\delta$) and CO_2 sorption capacities of the SCFN materials were highly sensitive to both the reducing environment. As the B-site gets increasingly reduced, more A-site oxides are exposed to CO_2 for carbonation into ACO_3. Therefore, it is expected that the sorption capacity is positively correlated to $\Delta\delta$. To investigate this relationship, both packed bed and TGA experiments were conducted. From Figure 3(d), we can see that sorption capacity across the SCFN

compositions trends positively with $\Delta\delta$. Interestingly, a volcano-like relationship can be seen. An increase from 30% to 40% Sr doping in the A-site substantially improves sorption capacity and oxygen donation, followed by a steady decrease and stabilization past 50% doping. The trends in sorption capacity from the TGA experiments are mirrored by those measured from the SESRG reactor experiments (see Table S2).

To assess whether sintering phenomena is taking place between cycles, fresh, reduced, and regenerated SCFN-5591 samples were imaged and mapped using SEM-EDS. From the SEM images (Figure 4) we see that no significant particle agglomeration occurs between the fresh, reduced, and regenerated samples. Between the fresh (Figure 4 (a/b)) and reduced (Figure 4 (c/d)) samples, there is a noticeable increase in surface texture – likely attributable to the formation of carbonates. Surface elemental mapping with EDS depicts a mostly homogenous distribution of A-and-B-site elements, with the exception of Ni, which appears to aggregate in clusters for both fresh and regenerated SCFN-5591 samples (Figure 5). XRD patterns of fresh SCFN samples reveal small amounts of NiO, suggesting that exsolution of Ni cations from the B-site of perovskite occurred during the 1,000 ˚C calcination (Figure 6).

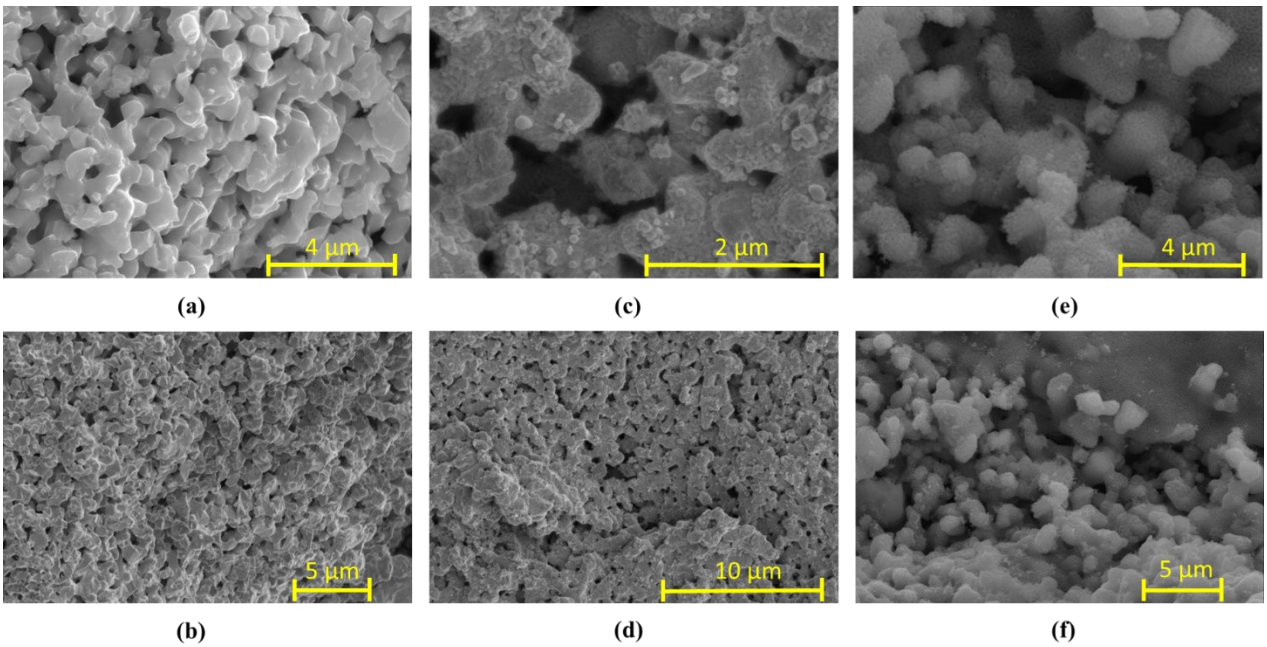

Figure 4. SEM images at varying magnifications for (a & b) fresh; (c & d) reduced; and (e & f) regenerated samples of SCFN-5591 obtained from the SESRG reactor experiments.

Additionally, the regenerated sample appears to have larger pore widths than its fresh counterpart from the SEM images. To confirm this observation, pore size distributions for fresh and reactor cycled (35 times) SCFN-5591 were obtained via BJH. The BET surface areas between the fresh sample (3.4 $m^2 \cdot g^{-1}$) and the spent sample (3.1 $m^2 \cdot g^{-1}$) are similar, but the average pore volume significantly increases from 10.4 nm for the fresh sample to 18.8 nm for the spent sample. Too small pores will be easily blocked by the carbonates, thus, the increase in average pore width could partially explain the increase in sorption capacity witnessed in the first ten cycles of SESRG reactions for this material (Figure 4(a)).

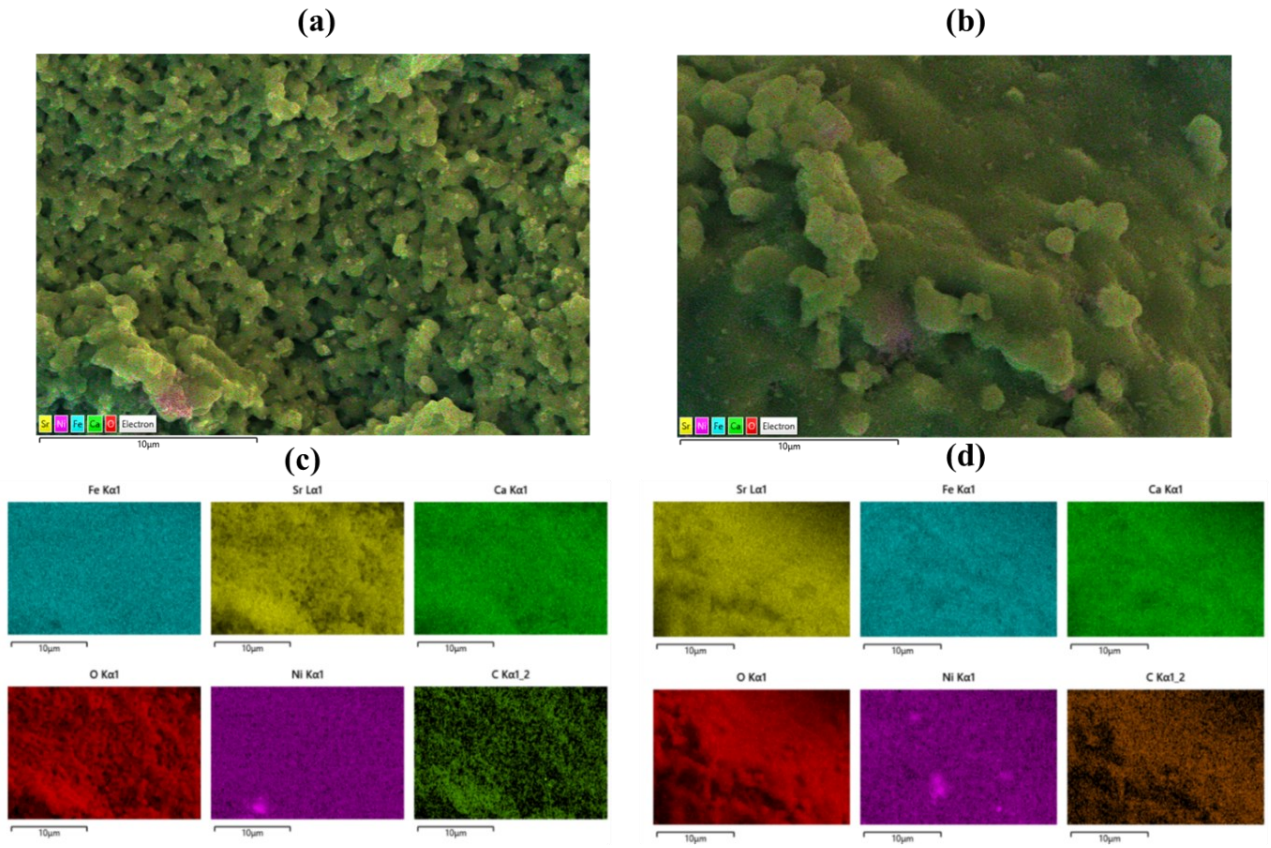

Figure 5. EDS mapping of (a & c) reactor-reduced and (b & d) regenerated SCFN-5591.

Phase reversibility and proposed reaction scheme

Evidence of SCFN's phase reversibility is also witnessed in phase characterization via powder XRD analysis. Figure 6 (a & b) displays the XRD patterns of fresh and spent samples of SCFN-4691 and 5591. The nearly perfect peak alignment of the samples pre-and post-15 cycles exhibits the superb durability and recyclability of SCFN. Small amounts of FeO and $SrCO_3$ can be observed in the post-15 cycled SCFN-4691 (Figure 6(a)), but this is likely due to an insufficiently long regeneration/decarbonation time in our reactor experiments. TGA experiments were used to provide a more idealized picture of the phase transitions occurring since the gaseous atmospheres could be more easily tuned, and the smaller sample mass (~50 mg) more uniformly reduced or reoxidized. These experiments, coupled with *ex-situ* XRD analysis, indicated that SCFN's extent of reduction, and therefore carbonate formation, is highly sensitive to the gas compositions in the reduction step, i.e., the reducing environment. Despite the differences in reduction environment between the TGA, which contains no steam, and the reactor, evidence of phase change within the TGA remains constructive for devising a pathway. Consider the XRD patterns in Figure 6 (c & d) comparing the extent of reduction of SCFN-3791 in a TGA vs. reactor environment. The greater extent of reduction seen in the TGA, shown in Figure 6(d), reveals the presence of FeO - indicating a greater B-site reduction to Fe^{2+} with correspondingly more pronounced carbonate, CaO and SrO peaks. The relatively lower extent of B-site cation reduction from the reactor samples could be the result of steam inhibition.

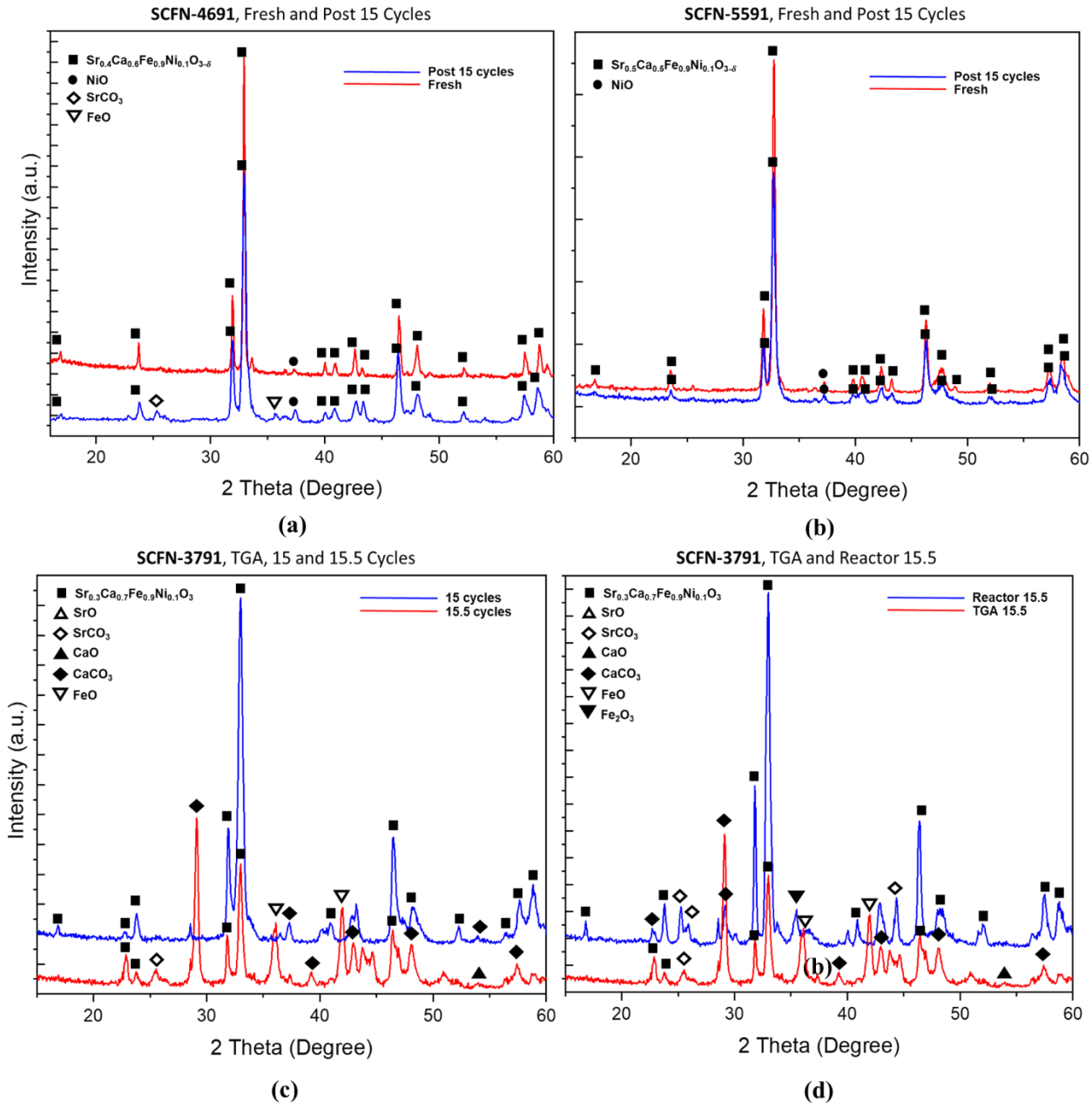

Figure 6. *Ex-situ* XRD patterns for fresh and post-15 reaction cycles of (a) SCFN-4691 and (b) SCFN-5591. After 15 reaction cycles, the characteristic perovskite peaks remained intact, signifying that the samples succeeded in reverting to their starting phase after decarbonation. SCFN-3791 XRD patterns showing (c) extent of reduction in TGA environment; and (d) comparison between extent of reduction between TGA environment and reactor environment. Note that 15.5 cycles indicates that the cycle was cut off after the reduction step. ICDD ref codes: $Sr_{0.5}Ca_{0.5}FeO_{2.5}$ (04-023-9930), NiO (00-001-1239), SrO (00-006-0520), $SrCO_3$ (04-013-9713), CaO (01-077-2010), $CaCO_3$ (04-016-9713), Fe_2O_3 (00-039-1346), FeO (04-008-2748).

In addition to revealing the dynamic phase transitions occurring under different gas atmospheres, *in-situ* XRD results further illustrate the difference in the extent of reduction between samples treated with solely H_2 vs. H_2/CO_2. Both samples of SCFN-5591 were exposed to the same volumetric concentration of H_2 (17.75%), with the exception that one also had an additional 4.75% CO_2 flowed in during the 570 ˚C reduction step (the balance Ar). Interestingly, the diffraction

pattern of the sample treated with both H_2/CO_2 showed a visible increase in peak intensity around $2\theta = 32.4^{\circ}$ as the temperature increased under 10% O_2 (Figure 7(b)). Figure 7(c) more clearly shows that there is a shift from 32.44˚ to 32.35˚ of the major peak, likely due to slight temperature-induced lattice expansion. The gradual disappearance of the Fe_2O_3 peak located at ~35.7 ˚provides evidence that phase transition is indeed occurring as the B-site metal is oxidized to a higher valency than Fe^{3+}. In stark contrast, the contour plot for the H_2-pretreated sample in Figure 7(a) showed virtually no change in peak intensity, revealing that the sample was only marginally reduced. These results suggest that CO_2 and the carbonation reaction provide a driving force for the reduction of SCFN. The H_2/CO_2-reduced sample also shed light on the stability of the formed carbonates from the perovskite A-site. The $CaCO_3$ diffraction signal is very weak and disappears as soon as the temperature surpasses ~610 ˚C, whereas the $SrCO_3$ patterns remain apparent until ~750 ˚C.

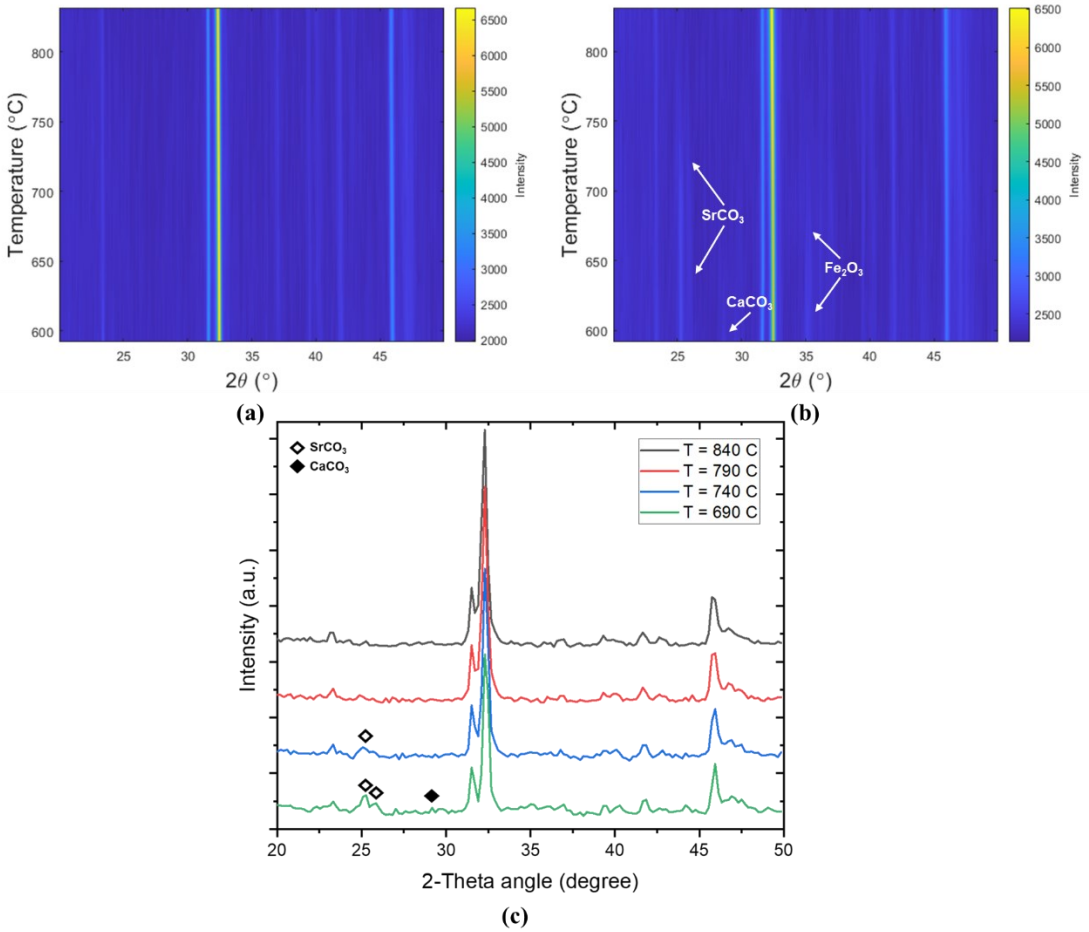

Figure 7. In-Situ XRD diffraction pattern contour plots of SCFN-5591 under a temperature ramp and 10% O_2/N_2 environment for samples (a) reduced with H_2 only and (b & c) reduced with both H_2 and CO_2.

From these XRD results, we propose the simplified SESRG reaction scheme involving the perovskite $(Sr/Ca)FeO_{3-\delta}$ illustrated by Reactions 11 and 12. The operating principle is that syngas produced from the reforming of glycerol reduces $(Sr/Ca)FeO_{3-\delta}$ to strontium oxide (SrO), calcium oxide (CaO) and reduced iron oxides. The coinciding WGS reaction converts some of the CO to CO_2, which is then taken up by SrO and CaO to form carbonates. This simultaneous carbonate

formation removes CO_2 to form conditioned syngas with a high H_2:CO ratio (see Reaction 11), and the subsequent decarbonation step in air releases the trapped CO_2 and regenerates the redox catalyst (see Reaction 12). The extent of perovskite reduction is represented by $\Delta\delta = \delta_2 - \delta_1$ where $\delta_1 = [0, 0.5]$ for the perovskite/Brownmillerite phase, and $\delta_2 = [0, 2]$ ranging from total to zero extent of B-site reduction. While for conventional oxidative steam reforming the presence of oxygen penalizes the H_2 yield, here the simultaneous carbonate formation compensates for that penalty by driving the WGS to produce more H_2. Assuming an ideal conversion of glycerol represented by Reaction 1, the amount of water consumed and the amount of H_2 produced can be related to the δ_1 and δ_2 via the stoichiometry of Reaction 11.

$$C_3H_8O_3 + [3(\delta_1 + \delta_2 - 1)]H_2O + 3(Sr/Ca)FeO_{3-\delta_1} \rightarrow$$
$$3(Sr/Ca)CO_3 + 3FeO_{\delta_2} + [4 + 3(\delta_1 + \delta_2 - 1)]H_2 \quad (11)$$

$$3(Sr/Ca)CO_3 + 3FeO_{\delta_2} + Air \rightarrow 3(Sr/Ca)FeO_{3-\delta_1} + 3CO_2 + N_2 \quad (12)$$

The formation of reduced A-site oxides (SrO, CaO) appears to be surface-sensitive and may not be easily identified by a bulk characterization technique like XRD for insufficiently reduced samples. Therefore, XPS was used to confirm the coexistence of these reduced oxides and their carbonates (results presented in the following section).

Surface chemical environment

XPS analysis was performed to determine the PTS surface chemical environment before and after the reduction/carbonation step. The Ca 2p, Fe 2p, and Sr 3d binding energy (BE) curves for fresh and reduced SCFN-5591 samples taken from the SESRG reactor are presented in Figure 8. *In-situ* XRD results for reduced SCFN-5591 samples revealed the presence of $SrCO_3$ and $CaCO_3$ (Figure 6), which were also detected by XPS. Due to its surface sensitivity, XPS also detected SrO and CaO species on the surface, which were not identified by XRD. Elemental analysis of the pre-reduction sample survey peak revealed that, despite the equimolar A-site composition, Ca was over twice as abundant as Sr on the surface at 17.86 atomic percentage (At%) versus 6.43%, The fresh sample also showed negligible surface Ni at only 0.04 At%. In contrast, the reduced sample showed a higher percentage of Ni at 0.14 At%, but this value was dwarfed by the 42.99 At% of C from surface carbonates. For the reduced sample, Ca remained the preferential surface species at 9.92 At% compared to 4.24% for Sr. This could be due to the smaller ionic radius of Ca^{2+} compared to Sr^{2+} - enabling faster diffusion to the surface.

The reduced SCFN-5591 Sr 3d spectrum was deconvoluted with three spin-orbital doublet pairs for Sr $3d_{3/2}$ and $3d_{5/2}$ BEs corresponding to three species: SrO, $SrCO_3$, and what is likely distorted lattice Sr within the Brownmillerite crystal (Sr_{latt}). In Figure 7(b), the doublets at 133.1 and 134.8 eV and 132.4 and 133.4 eV likely correspond to $SrCO_3$ and SrO, respectively [50, 51]. The main doublet feature of $SrFeO_3$ characteristic of the perovskite crystal, which is normally centered at ~133.8 eV [52], is now shifted to ~132 eV for the fresh sample in Figure 8(a) – likely due to the effects of Ca doping.

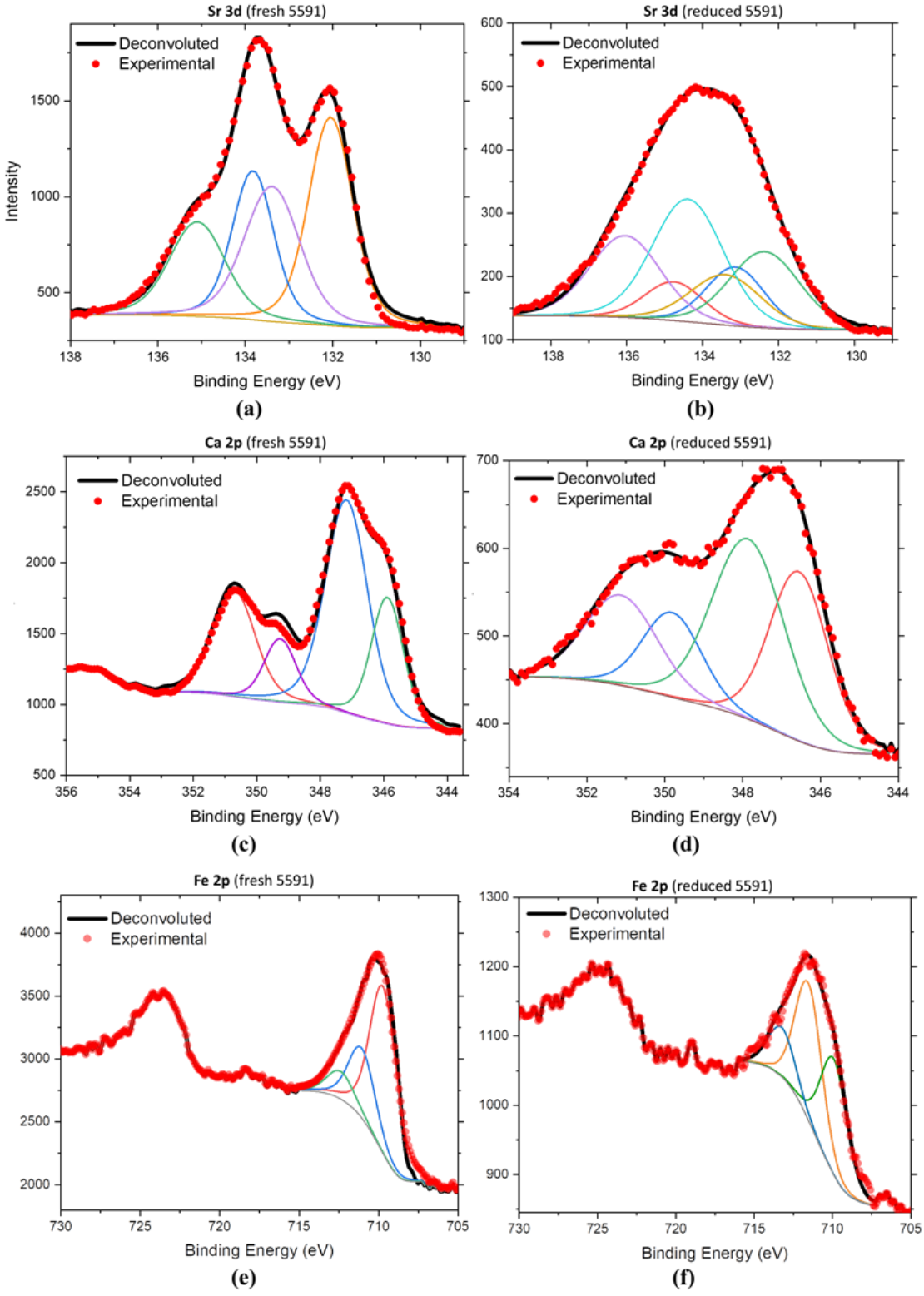

Figure 8. The core level XPS spectra for fresh and reduced SCFN-5591 for (a & b) Sr 3d, (c & d) Ca 2p, and (e & f) Fe 2p.

A similar deconvolution procedure was conducted for the Ca 2p peaks. For the reduced sample (Figure 8(d)), the doublets identified at 346.6/349.8 eV and 347.9/351.1 eV likely correspond to

CaO and $CaCO_3$, respectively [53,54]. The lack of lattice Ca peaks in the reduced sample deconvolution suggests that it was quickly carbonated or stabilized as CaO due to the B-site reduction. This may also relate to the lower kinetics of SrO carbonation at lower temperatures [55]. CaO has a very fast carbonation rate at lower temperatures. The proclivity for surface lattice Ca to carbonate explains the higher average CO_2 sorption capacities seen in SCFN-4691 and 5591 (see Table S2), however the lower sorption capacity of SCFN-3791 counters this trend – hinting at more complicated phenomena at play here than merely Ca molar percentage in the A-site.

The Fe $2p_{3/2}$ peaks were deconvoluted with three doublets. It is difficult for XPS to distinguish between the Fe^{3+} and Fe^{4+} valence states because both states exhibit a single peak for the $2p_{1/2}$ and $2p_{3/2}$ core levels [56]. However, features of the satellite peaks can be used to distinguish between the two. The Fe^{3+} spectrum should exhibit a more pronounced satellite peak at ~718 eV [56], which can be seen in Figure 8(f). For the reduced sample, peaks at 709.9 and 711.5 eV likely correspond to FeO and γ-Fe_2O_3 [57]. The higher BE peak at ~713 eV may be attributable to α-FeOOH, possibly formed after exposure to the ambient environment.

Conclusions

The current study demonstrated that perovskite-based phase transition sorbents (PTSs) can function as tri-functional materials capable of simultaneous catalysis, CO_2 sorption, and oxygen release under a cyclic scheme. Results from reactor testing revealed that all five compositions of SCFN achieved pre-breakthrough H_2 concentrations > 87 vol%, with SCFN-4691 and 5591 displaying relatively high hydrogen purities (95.6-97.3%) in the pre-breakthrough periods. TGA experiments revealed a direct proportionality between oxygen release ($\Delta\delta$) and CO_2 sorption capacity, confirming the synergistic relationship between B-site reduction and A-site carbonation. A combination of performance results and *ex-situ* XRD analysis showcased the longevity and phase recyclability of the SCFN materials.

A simplified reaction scheme has been proposed on the basis of *in-situ* XRD and XPS characterizations in which B-site reduction promotes the formation of A-site oxides on the surface (e.g., SrO and CaO) that are subsequently carbonated (and vice versa). *In-situ* XRD patterns confirmed that the formation of carbonates is fully reversible. SEM-EDS imaging coupled with BET analysis brought to light a favorable increase in average pore width on the surface of the PTS after cycling – showing that not only had sintering not occurred, but that in-fact the porosity of the material slightly improved. The confluence of these performance results and characterizations supports the continued investigation of perovskite oxides as viable PTS materials for a slew of possible sorption enhancement applications.

Associated Content

Supporting Information

The Supporting Information is available free of charge at: *insert link here*

A representative TGA profile showing the weight change of SCFN during the reduction and decarbonation steps (Figure S1), SESRG performance data over cycle number for five compositions (Figure S2), H_2 selectivity and yields of SCFN compounds compared to equilibrium conditions for oxidative steam

reforming of glycerol (Figure S3), TGA feed concentrations for reduction step by SCFN composition (Table S1), Summary of reactor performance data for various SCFN compositions (Table S2), XPS peak parameters for fresh and reduced SCFN-5591 samples (Table S3).

Acknowledgments

This work was supported by the U.S. Department of Energy Office of Energy Efficiency & Renewable Energy (No. EE0008809) and US National Science Foundation (CBET- 1923468). XPS experiments were performed in part at the Duke University Shared Materials Instrumentation Facility (SMIF), a member of the North Carolina Research Triangle Nanotechnology Network (RTNN), which is supported by the National Science Foundation as part of the National Nanotechnology Coordinated Infrastructure (NNCI). We also acknowledge the use of the Analytical Instrumentation Facility (AIF) at North Carolina State University, which is supported by the State of North Carolina and the National Science Foundation.

Conflict of Interest

The authors declare no conflict of interest.

References

1. Ki-Won, J. Roh, H-S. Kim, K-S. Ryu, J-S. Lee, K-W. Catalytic investigation for Fischer–Tropsch synthesis from bio-mass derived syngas. *Appl. Catal. A: Gen.* **2004**, *259*, 221-226. https://doi.org/10.1016/j.apcata.2003.09.034
2. Simpson, A.P. Lutz, A.E. Exergy analysis of hydrogen production via steam methane reforming. *Int. J. Hydrog. Energy.* **2007**, *32*, 4811-4820. https://doi.org/10.1016/j.ijhydene.2007.08.025
3. Gangadharan, P., Kanchi, K.C. Lou, H.H. Evaluation of the economic and environmental impact of combining dry reforming with steam reforming of methane. *Chem Eng Res Des.* **2012**, *90*, 1956-1968. https://doi.org/10.1016/j.cherd.2012.04.008
4. Rezaei, E. Dzuryk, S. Techno-economic comparison of reverse water gas shift reaction to steam and dry methane reforming reactions for syngas production. *Chem Eng Res Des.* **2019**, *144*, 354-369. https://doi.org/10.1016/j.cherd.2019.02.005
5. Adris, A.M. Pruden, B.B., Lim, C.J. Grace, J.R. On the Reported Attempts to Radically Improve the Performance of the Steam Methane Reforming Reactor. *Can J Chem Eng*. **1996**, *74*, 177-186. https://doi.org/10.1002/cjce.5450740202
6. Adeniyi, A.G. Ighalo, J.O. A review of steam reforming of glycerol. *Chem. Pap.* **2019**, *73*, 2619-2635. https://doi.org/10.1007/s11696-019-00840-8
7. Valliyappan, T.Bakhshi, N.N. Dalai, A.K. Pyrolysis of glycerol for the production of hydrogen or syn gas. *Bioresour Technol*. **2008**, *99*, 4476-83. https://doi.org/10.1016/j.biortech.2007.08.069
8. Fernández, Y. Arinillas, A. Díez, M.A. Pis, J.J. Menéndez, J.A. Pyrolysis of glycerol over activated carbons for syngas production. *J Anal Appl Pyrolysis*. **2009**, *84*, 145-150. https://doi.org/10.1016/j.jaap.2009.01.004
9. Buffoni, I.N. Pompeo, F. Santori, G.F. Nichio, N.N. Nickel catalysts applied in steam reforming of glycerol for hydrogen production. *Catal. Commun.* **2009**, *10*, 1656-1660. https://doi.org/10.1016/j.catcom.2009.05.003
10. Jiang, B. Dou, B. Song, Y. Zhang, C. Du, B. Chen, H. Wang, C. Xu, Y. Hydrogen production from chemical looping steam reforming of glycerol by Ni-based oxygen carrier in a fixed-bed reactor. *Chem. Eng. J.* **2015**, *280*, 459-467. https://doi.org/10.1016/j.fuel.2016.06.061

11. Luo, N. Fu, X. Cao, F. Xiao, T. Edwards, P.P. Glycerol aqueous phase reforming for hydrogen generation over Pt catalyst – Effect of catalyst composition and reaction conditions. *Fuel*. **2008**, *87*, 3483-3489. https://doi.org/10.1016/j.fuel.2008.06.021
12. Kale, G.R. Kulkarni, B.D. Thermodynamic analysis of dry autothermal reforming of glycerol. *Fuel. Process. Technol.* **2010**, *91*, 520-530. https://doi.org/10.1016/j.fuproc.2009.12.015
13. Authayanun, S. Arpornwichanop, A. Paengjuntuek, W. Assabumrungrat, S. Thermodynamic study of hydrogen production from crude glycerol autothermal reforming for fuel cell applications. *Int. J. Hydrog. Energy.* **2010**, *35*, 6617-6623. https://doi.org/10.1016/j.ijhydene.2010.04.050
14. Garcia, L. French, R, Czernik, S. Chornet, E. Catalytic steam reforming of bio-oils for the production of hydrogen: effects of catalyst composition. *Appl. Catal. A: Gen.* **2000**, *201*, 225-239. https://doi.org/10.1016/S0926-860X(00)00440-3
15. S. Adhikari, Fernando, S.D. Filip To, S.D., Bricka, R.M. Steele, P.H. Haryanto, A. Conversion of Glycerol to Hydrogen via a Steam Reforming Process over Nickel Catalysts. *Energy & Fuels*. **2008**, *22*, 1220–1226. https://doi.org/10.1021/ef700520f
16. Sharma, P.O. Swami, S. Goud, S. Abraham, M.A. Catalyst development for stable hydrogen generation during steam reforming of renewable and nonrenewable resources. *Environ. Prog.* **2008**, *27,* 22-29. https://doi.org/10.1002/ep.10234
17. Adhikari, S. Fernando, S.D. Haryanto, A. Hydrogen production from glycerin by steam reforming over nickel catalysts. *Renew. Energy*. **2008**, *33*, 1097-1100. https://doi.org/10.1016/j.ijhydene.2018.06.048
18. Delparish, A., Koc, S. Caglayan, B.S., Avci, A.K. Oxidative steam reforming of glycerol to synthesis gas in a microchannel reactor. *Catal. Today.* **2019**, *323*, 200-208. https://doi.org/10.1016/j.cattod.2018.03.047
19. He, L., Manuel Salamnaca Parra, J. Blekkan, E.A. Chen, D. Towards efficient hydrogen production from glycerol by sorption enhanced steam reforming. *Energy Envion. Sci*. **2010**, *3*, 1046-1056. **DOI** https://doi.org/10.1039/B922355J
20. Iliuta, I., Radfarina, H.R. Iliuta, M.C. Hydrogen Production by Sorption-Enhanced Steam Glycerol Reforming: Sorption Kinetics and Reactor Simulation. *AIChE J.* **2013**, *59*, 2105-2118. https://doi.org/10.1002/aic.13979
21. Li, H. Tian, H. Chen, S. Sun, Z. Liu, T. Liu, R. Assabumrungrat, S. Saupsor, J. Mu, R. Pei, C. Gong, J. Sorption enhanced steam reforming of methanol for high-purity hydrogen production over Cu-MgO/Al_2O_3 bifunctional catalysts. *Appl. Catal. B.* **2020**, *276*, 119052-119061. https://doi.org/10.1016/j.apcatb.2020.119052
22. Lima da Silva, A. Müller, I.L. Hydrogen production by sorption enhanced steam reforming of oxygenated hydrocarbons (ethanol, glycerol, n-butanol and methanol): Thermodynamic modelling. *Int. J. Hydrog. Energy.* **2011**, *36*, 2057-2075. https://doi.org/10.1016/j.ijhydene.2010.11.051
23. Wang, S. Yang, S. Xu, S. Zhang, K. Li, B. *Int. J. Hydrog. Energy.* Assessment of sorption-enhanced crude glycerol steam reforming process via CFD simulation. **2018**, *43*, 14996-15004. https://doi.org/10.1016/j.ijhydene.2018.06.053
24. Dang, C. Yu, H. Wang, H. Peng, F. Yang, Y. A bi-functional Co–CaO–$Ca_{12}Al_{14}O_{33}$ catalyst for sorption-enhanced steam reforming of glycerol to high-purity hydrogen. *Chem. Eng. J.* **2016**, *286*, 329-338. https://doi.org/10.1016/j.cej.2015.10.073
25. Dang, C. Li, Y. Yusuf, S.M., Cao, Y. Wang, H. Yu, H. Peng, F. Li, F. Calcium cobaltate: a phase-change catalyst for stable hydrogen production from bio-glycerol. *Energy Envion. Sci*. **2018**, *11*, 660-668. https://doi.org/10.1039/C7EE03301J
26. Li, B. Shuai, W. Yang, X. Wu, Q. He, Y. Thermodynamic evaluation of sorption-enhanced chemical looping gasification with coal as fuel. *Int. J. Hydrog. Energy.* **2020**, *45*, 21186-21194. https://doi.org/10.1016/j.ijhydene.2020.05.205
27. Solis, B.H., Cui, Y. Weng, X. Seifert, J. Schauermann, S. Sauer, J. Shaikhutdinov, S. Freund, H-J. Initial stages of CO_2 adsorption on CaO: a combined experimental and computational study. *Phys. Chem. Chem. Phys*. **2017**, *19*, 4231-4242. https://doi.org/10.1039/C6CP08504K

28. Xu, Y., Luo, C. Zheng, Y. Ding, H. Wang, Q. Shen, Q. Li, X. Zhang, L. Characteristics and performance of CaO-based high temperature CO_2 sorbents derived from a sol–gel process with different supports. *RSC Adv*. **2016**, *6*, 79285-79296. https://doi.org/10.1039/C6RA15785H
29. Fennell, P.S. Pacciani, R. Dennis, J. S. Davidson, J.F. Hayhurst, A.N. The Effects of Repeated Cycles of Calcination and Carbonation on a Variety of Different Limestones, as Measured in a Hot Fluidized Bed of Sand. *Energy & Fuels*. **2007**, *21*, 2072-2081. https://doi.org/10.1021/ef060506o
30. H. Lu, Reddy, E.P. Smirniotis, P.G. Calcium Oxide Based Sorbents for Capture of Carbon Dioxide at High Temperatures. *Ind. Eng. Chem. Res.* **2006**, *45*, 3944-3949. https://doi.org/10.1021/ie051325x
31. Sultana, K.S., Trung Tran, D. Walmsley, J.C. Rønnig, M. Chen, D. CaO Nanoparticles Coated by ZrO_2 Layers for Enhanced CO_2 Capture Stability. *Ind. Eng. Chem. Res*. **2015**, *54*, 8929-8939. https://doi.org/10.1021/acs.iecr.5b00423
32. Lan, P. Wu, S. Mechanism for self-reactivation of nano-CaO-based CO_2 sorbent in calcium looping. *Fuel*. **2015**, *143*, 9-15. https://doi.org/10.1016/j.cattod.2015.05.026
33. Xu, P., Zhu, Z. Zhao, C. Cheng, Z. Catalytic performance of Ni/CaO-$Ca_5Al_6O_{14}$ bifunctional catalyst extrudate in sorption-enhanced steam methane reforming. *Catal. Today*. **2016**, *259*, 347-353. https://doi.org/10.1016/j.cattod.2015.05.026
34. Wu, S.F. Wang, L.L. Improvement of the stability of a ZrO_2-modified Ni–nano-CaO sorption complex catalyst for ReSER hydrogen production. *Int. J. Hydrog. Energy*. **2010**, *35*, 6518-6524. https://doi.org/10.1016/j.ijhydene.2010.03.120
35. Xie, M., Zhou, Z. Qi, Y. Cheng, Z. Yuan, W. Sorption-enhanced steam methane reforming by in situ CO_2 capture on a CaO–$Ca_9Al_6O_{18}$ sorbent. *Chem. Eng. J.* **2012**, *207-208,*142-150. https://doi.org/10.1016/j.cej.2012.06.032
36. Armutlulu, A., Naeem, A.W. Liu, H-J. Kim, S.M. Kierzkowska, A. Fedorov, A., Müller, C.R. Multishelled CaO Microspheres Stabilized by Atomic Layer Deposition of Al_2O_3 for Enhanced CO_2 Capture Performance. *Adv Mater*. **2017**, *29*, 1702896-1702907. https://doi.org/10.1002/adma.201702896
37. Nishihata, Y. Mizuki, J. Akao, T. Tanaka, H. Uenishi, M. Kimura, M. Okamoto, T. Hamada, N. Self-regeneration of a Pd-perovskite catalyst for automotive emissions control. *Nature*. **2002**, *418*, 164-167. https://doi.org/10.1038/nature00893
38. Zhao, M. Shi, J. Zhong, X. Tian, S. Blamey, J. Jiang, J. Fennell, P.S. A novel calcium looping absorbent incorporated with polymorphic spacers for hydrogen production and CO_2 capture. *Energy Environ. Sci*. **2014**, *7*, 3291-3295. https://doi.org/10.1039/C4EE01281J
39. Gu, H. Gao, Y. Iftikhar, S. Li, F. Ce stabilized Ni-SrO as a catalytic phase transition sorbent for integrated CO_2 capture and CH_4 reforming. *J. Mater. Chem. A*. **2022**, *10*, 3077-3085. https://doi.org/10.1039/D1TA09967A
40. Bulfin, B., Vieten, J. Starr, D.E. Azarpira, A. Zachäus, C. Hävecker, M. Skorupska, K. Schmücker, M. Roeb, M. Sattler, C. Redox chemistry of $CaMnO_3$ and $Ca_{0.8}Sr_{0.2}MnO_3$ oxygen storage perovskites. *J. Mater. Chem. A*. **2017**, *5*, 7912-7919. https://doi.org/10.1039/C7TA00822H
41. Galinsky, N., Sendi, M. Bowers, L. Li, F. CaMn1−B O3− (B = Al, V, Fe, Co, and Ni) perovskite based oxygen carriers for chemical looping with oxygen uncoupling (CLOU). *Appl. Energy*. **2016**, *174*, 80-87. https://doi.org/10.1016/j.apenergy.2016.04.046
42. Ji, Q. Bi, L. Zhang, J. Cao, H. Zhao, X.S. The role of oxygen vacancies of ABO_3 perovskite oxides in the oxygen reduction reaction. *Energy Environ. Sci*. **2020**, *13*, 1408-1428. https://doi.org/10.1039/D0EE00092B
43. Mishra, A. Li, T. Li, F. Santiso, E. Oxygen Vacancy Creation Energy in Mn-Containing Perovskites: An Effective Indicator for Chemical Looping with Oxygen Uncoupling. *Chem. Mater*. **2018**, 31, 689-698. https://doi.org/10.1021/acs.chemmater.8b03187
44. Marek, E. Hu, W. Gaultois, M. Grey, C.P. Scott, S.A. The use of strontium ferrite in chemical looping systems. *Appl. Energy*. **2018**, *223*, 369-382. https://doi.org/10.1016/j.apenergy.2018.04.090

45. Luongo, G. Donat, F. Müller, C.R. Structural and thermodynamic study of Ca A- or Co B-site substituted $SrFeO_{3-\delta}$ perovskites for low temperature chemical looping applications. *Phys. Chem. Chem. Phys*. **2020**, *22*, 9272-9282. https://doi.org/10.1039/D0CP01049A
46. Wang, X. Krzystowczyk, E. Dou, J. Li, F. Net Electronic Charge as an Effective Electronic Descriptor for Oxygen Release and Transport Properties of $SrFeO_3$-Based Oxygen Sorbents. *Chem. Mater*. **2021**, *33*, 2446-2456. https://doi.org/10.1021/acs.chemmater.0c04658
47. Zhu, X. Imtiaz, Q. Donat, F. Müller, C.R. Li, F. Chemical looping beyond combustion – a perspective. *Energy Environ. Sci*. **2020**, *13*, 772-804. https://doi.org/10.1039/C9EE03793D
48. Liu, X. Hong, R. Tian, C. Tolerance factor and the stability discussion of ABO_3-type ilemite. *J Mater Sci: Mater Electron*. **2009**, *20*, 323-327. https://doi.org/10.1007/s10854-008-9728-8
49. Whangbo, M.H. Koo, H.J. Villesuzanne, A. Pouchard, M. Effect of Metal−Oxygen Covalent Bonding on the Competition between Jahn−Teller Distortion and Charge Disproportionation in the Perovskites of High-Spin d^4 Metal Ions $LaMnO_3$ and $CaFeO_3$. *Inorganic Chemistry*. **2002**, *41*, 1920-1929. https://doi.org/10.1021/ic0110427
50. Vasquez, R.P. X-ray photoelectron spectroscopy study of Sr and Ba compounds. *J. Electron Spectrosc. Relat. Phenom.* **1991**, *56*, 217-240. https://doi.org/10.1016/0368-2048(91)85005-E
51. Sosulnikov, M.I. Teterin, Y.A. X-ray photoelectron studies of Ca, Sr and Ba and their oxides and carbonates. *J. Electron Spectrosc. Relat. Phenom.* ***1992***, 59, 111-126. https://doi.org/10.1016/0368-2048(92)85002-O
52. Ghaffari, M. Huang, H. Tan, O.K. Shannon, M. Band gap measurement of $SrFeO_{3-\delta}$ by ultraviolet photoelectron spectroscopy and photovoltage method. *CrystEngComm*. **2012**, *14*, 7487-7492. **DOI** https://doi.org/10.1039/C2CE25751C
53. Wang, Y. Zuo, Y. Adsorption and Inhibition Behavior of Calcium Lignosulfonate on Steel in NaCl + $Ca(OH)_2$ Solutuons with Different pH Values. Int. *J. Electrochem. Sci*. **2016**, *11*, 6976-6992. https://doi.org/10.1016/j.apsusc.2016.04.013
54. Ni, M. Ratner, B.D. Differentiation of Calcium Carbonate Polymorphs by Surace Analysis Techniques - An XPS and TOF-SIMS study. *Surf Interface Anal*. **2008**, *40*, 1356-1361. https://doi.org/10.1002/sia.2904
55. Ghirbaei, S.Z. Ebrahim, H.A. Carbonation reaction of strontium oxide for thermochemical energy storage and CO_2 removal applications: Kinetic study and reactor performance prediction. *Appl. Energy*. **2020**, *277,* 115604-115616. https://doi.org/10.1016/j.apenergy.2020.115604
56. Rogge, P.C. Chandrasena, R.U. Cammarata, A. Green, R.J. Shafer, P. Lefler, B.M. Huon, A. Arab, A. Arenholz, E. Lee, H.N. Lee, T-L. Nemšák, S. Rondinelli, J.M. Gray, May, S.J. Electronic structure of negative charge transfer $CaFeO_3$ acorss the metal-insulator transition. *Phys. Rev. Materials*. **2018**, *2*, 015002-015010. https://doi.org/10.48550/arXiv.1801.05374
57. Grosvenor, A.P. Kobe, B.A. Biesinger, M.C. McIntyer, N.S. Investigation of multiplet splitting of Fe 20 XPS spectra and bonding in iron compounds. *Surf Interface Anal*. **2004**, *36*, 1564-1574. https://doi.org/10.1002/sia.1984

For Table of Contents Use Only

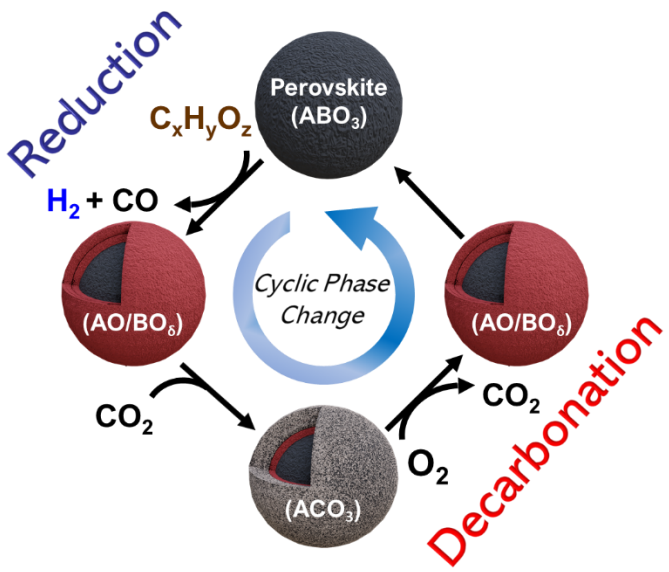

Phase transition sorbents enable cyclical, *in-Situ* CO_2 capture for production of H_2-rich gas from renewable carbonaceous sources.